Supporting Information for, "Stopping the Flood: Could We Use Targeted Geoengineering to Mitigate Sea Level Rise?", by M.J. Wolovick and J.C. Moore

May 6, 2018

1 Model Description

1.1 Ice Model

We use a vertically and laterally integrated Shallow Shelf Approximation (SSA) flowband model. The effects of side drag and flow convergence are parameterized through a variable flowband width, W. The equations for conservation of mass and momentum are, respectively,

$$\frac{\partial H}{\partial t} = \frac{1}{W}\frac{\partial}{\partial x}(uHW) + \dot{b} - \dot{m}, \tag{1}$$

$$\frac{\partial}{\partial x}\left(HW\mu\frac{\partial u}{\partial x}\right) - W\rho_i gH\frac{\partial S}{\partial x} - W\tau_b - 2H\left(\frac{u}{A_{side}W}\right)^{1/n} = 0 \tag{2}$$

where x is the along-flow coordinate, t is time, H is the ice thickness, u is the vertically and laterally averaged velocity, $\dot{b}$ is the surface mass balance, $\dot{m}$ is the basal melt rate, ρ_i is ice density, g is the acceleration due to gravity, S is the surface elevation, μ is the effective viscosity, A_{side} is a rate factor for side drag, τ_b is basal drag, and $n = 3$ is the rheological exponent for ice. Effective viscosity is defined by,

$$\mu = 2\left(A_{long}\right)^{-1/n}\left(\dot{\epsilon}_{eff}\right)^{\frac{1-n}{n}}, \tag{3}$$

$$\dot{\epsilon}_{eff} = \sqrt{\left(\frac{\partial u}{\partial x}\right)^2 + \left(\frac{u}{W}\right)^2}, \tag{4}$$

where $\dot{\epsilon}_{eff}$ is the effective strain rate, and A_{long} is the rate factor for longitudinal stresses. We included the cross-flow strain rate in the equation for effective viscosity because including an additional non-zero term has the effect of stabilizing the numerical solution in the vicinity of local velocity extrema without resorting to an arbitrary stabilizing term. Local velocity extrema are more likely with flowband geometries based on real glaciers that include topographic variability, as opposed to idealized configurations. The model uses a separate rate factor for longitudinal stress and lateral drag to parameterize the effect of shear margins, where ice rheology can be very different from surrounding regions. The best-fit rate factors are solved for simultaneously with the inversion that solves for the best-fit basal drag (Section 1.4).

Surface elevation is given by,

$$S = max\left[B + H, \left(1 - \frac{\rho_i}{\rho_w}\right)H\right] \tag{5}$$

where B is bedrock elevation and ρ_w is the density of seawater. Sub-grid grounding line position is interpolated using a cubic scheme based on the two cells upstream and downstream of the grounding line. In the event that the glacier geometry contains multiple grounding lines, sub-grid interpolation is performed for all of them. The interpolated position is used to partition basal drag and basal melt in partially grounded cells. Basal drag is given by a Weertman-type (Weertman, 1957) power-law sliding rule,

$$\tau_b = \tau_0 \left(\frac{u}{u_0}\right)^{1/r} \tag{6}$$

where $\tau_0(x)$ is a spatially variable stress scale, $u_0(x)$ is a spatially variable velocity scale, and r is a spatially invariant slip exponent. These parameters are related to the rate factor in the classic form of Weertman-type sliding ($u = C\tau_b^r$) by: $C = \tau_0/u_0^r$. We expressed the sliding law this way so that experiments could change the slip exponent without having to solve for a new rate factor or change the units. The sliding law was constrained to match present-day surface velocities (Rignot et al., 2011). The inversion (Section 1.4) fit observed width-averaged velocities using a linear sliding rule with a spatially variable rate factor and two additional scalar parameters, A_{long} and A_{side}. Once the best-fit linear sliding rule was obtained, the model velocity and basal drag were taken to represent $u_0(x)$ and $\tau_0(x)$. This procedure ensured that all values of r fit present-day surface velocities. We varied r in different model experiments to represent the difference between viscous and plastic beds, but the model does not represent spatial variations in r that could be caused by the uneven distribution of subglacial sediments, nor does it represent temporal changes in the distribution of subglacial water.

1.2 Plume Model

The ice model is coupled to a bouyant turbulent plume model for determining the melt rate under floating ice shelves and at the vertical calving front. The plume model (Jenkins, 1991, 2011) solves the equations for the conservation of mass, momentum, heat, and salt. Those equations are,

$$\frac{1}{W}\frac{d}{ds}(dvW) = \dot{e} + \dot{m}, \tag{7}$$

$$\frac{1}{W}\frac{d}{ds}\left(dv^2W\right) = d\left(\frac{\rho_a - \rho}{\rho_0}\right) gsin(\alpha) - c_d v^2, \tag{8}$$

$$\frac{1}{W}\frac{d}{ds}(dvTW) = \dot{e}T_a + \dot{m}T_f - c_d^{1/2} v\Gamma_{TS}(T - T_f), \text{and} \tag{9}$$

$$\frac{1}{W}\frac{d}{ds}(dvSW) = \dot{e}S_a, \tag{10}$$

where s is the along-plume coordinate, measured along the underside of the floating shelf and up the vertical calving front, d is the thickness of the plume, v is the velocity of the plume, T and S are the temperature and salinity of the plume, $\dot{e} = e_0 v^* sin(\alpha)$ is the entrainment rate, e_0 is the dimensionless entrainment constant, $v^* = \sqrt{v^2 + v_{tidal}^2}$ is the effective mixing velocity, $v_{tidal} = 10$ cm/s is the assumed tidal velocity, α is the slope of the ice bottom, c_d is a drag coefficient, Γ_{TS} is the Stanton number, and subscript a indicates ambient water properties, which are allowed to vary vertically. The Stanton number, representing exchange between the laminar ice-contact boundary layer and the turbulent plume, is poorly constrained (Jenkins, 2011). We calibrated the Stanton number separately for each glacier geometry (Section 1.3) by letting the model run freely for 10 years and selecting the value that best preserved the relative shape of the ice shelf, defined as the ratio of the ice bottom slope near the grounding line to the average slope over the whole ice shelf. We used the relative shape of the ice shelf to calibrate the plume model in order to strike a balance between an over-aggressive plume that concentrates too much melt near the grounding and a weak plume that spreads out the melt too much over the shelf bottom, while still allowing the mean melt rate under the shelf to be out of balance in the initial condition. The Stanton numbers we derived in this way were within a factor of 2 of the number recommended by Jenkins (Jenkins, 2011). The far-field ocean profiles are converted into ambient profiles at the ice-ocean interface by assuming that the water properties at the depth of the sill top overflow and fill the basin behind the sill. In experiments without an artificial sill the maximum bedrock elevation seaward of the grounding line was used instead of the sill top. The conservation equations have been modified from Jenkins (Jenkins, 1991, 2011) to account for variable flowband width. Melt rate is given by the simplified two-equation model (Jenkins, 2011),

$$\dot{m} = \frac{c_w v^* \Gamma_{TS} \left(T - T_f\right)}{L + c_i \left(T_f - T_i\right)}, \text{and} \tag{11}$$

$$T_f = \lambda_1 S + \lambda_2 + \lambda_3 z, \tag{12}$$

where c_w and c_i are the specific heats of water and ice, T_i is the temperature of the ice, λ_1–λ_3 are the coefficients of a linear equation of state, and z is the depth of the plume at that point. The boundary conditions at the grounding line are zero salinity, temperature equal to the melting point, and a flux given by integrating basal and surface melt across the grounded domain. A constant basal melt rate of 1 mm/yr was used, which is probably representative of many outlet glacier catchment basins, while surface melt followed an assumed seasonal cycle with a 4 month ablation season every year. We ran an additional test in which the grounded melt rate was set to 20 mm/yr, closer to the mean value for the Thwaites basin (Joughin et al., 2009). For the test we reran the warming and large sill scenarios for one experiment. Increasing the grounded melt rate by a factor of 20 caused the collapse to accelerate by 10 years in the warming scenario; the sill scenario was still a successful intervention, with the model glacier gaining mass after the sill was built. The plume model operated on a separate grid from the ice model and melt rate was interpolated back to the ice grid in a mass-conserving manner. At the corner between the underside of the floating ice shelf and the vertical calving front the properties of the under-shelf plume are used as boundary conditions for the calving front plume.

1.3 Flowband Construction

In order to create flowband models representing a real glacier, it is necessary to convert 2D maps of various ice properties– surface and basal geometry, velocity, and surface mass balance– into 1D along-flow profiles. Interpolating along a centerline is unlikely to produce results that are representative of the full glacier (Sergienko, 2012), so some form of across-flow averaging must be used. There are two main steps needed to perform an across-flow averaging: 1) the lateral boundaries of the glacier must be defined, and 2) an along-flow distance must be computed. For complex real geometries, neither of these steps are trivial. We used two sets of lateral boundaries, a wide set and a narrow set. We drew the wide boundaries to include all major tributaries, as well as the slow-flowing areas in between the tributaries. We drew the narrow set to only include the central trunk of the glacier. The narrow boundaries provide a better representation of the dynamically important fast-flowing trunk of the glacier, but at the price of drawing a large fraction of their mass input from unmodeled tributaries entering the lateral margins of the flowband. The wide boundaries include very little unmodeled mass inputs, but at the price of averaging together bed topography in deep fast-flowing troughs with bed topography in the intervening shallow slow-flowing areas. To compromise between these two extremes, We generated a third set of flowbands using the wide boundaries, but with bed and surface geometry generated from a flux-weighted average in the across-flow dimension, rather than a simple average. In all nomenclature used in this paper, "A" flowbands have wide boundaries with unweighted-average topography, "B" flowbands have narrow boundaries, and "C" flowbands have wide boundaries with flux-weighted topography. In general, the B and C flowbands had deeper beds and more overdeepened geometries than the A flowbands.

Once we defined the flowband boundaries, we computed along-flow distance by first defining a flux gate near the calving front and then integrating the velocity direction field upstream from that line. We used a combined velocity field constructed by merging the observed surface velocity with modelled balance velocity in order to produce a final product without gaps. All of the flowbands continued beyond the present-day calving front in order to permit the model glacier to advance. We used the orientation of the flowband boundaries to produce the direction field necessary to continue the distance integration beyond the present–day calving front. Once along-flow distance was defined throughout the flowband, we performed the across-flow averaging using a 5km along-flow smoothing. Flowband width was computed in an area-conserving manner, such that $\int W(x)dx$ computed in the along-flow coordinate is equal to the area enclosed by the flowband boundaries on the map.

1.4 Velocity Inversion

We solve for a best-fitting sliding rule by fitting to width-averaged surface velocity computed from the merged velocity field (observations (Rignot et al., 2011) with balance velocity to fill the gaps) during flowband construction. We solved for both a spatially variable sliding coefficient in a linear Weertman-type sliding law ($C(x)$) and spatially invariant rate factors for side drag and longitudinal stress (A_{long} and A_{side}). We used an evolutionary algorithm to find the inputs that minimized a cost function. Starting from an initial guess, the evolutionary algorithm creates a new population of input models at every generation from random red noise mutations to the previous generation. After evaluating the cost function for each population member, the algorithm discards the worst half of the population and then creates a new population from the best half. An example of the convergence behavior of the evolutionary algorithm is shown in Figure S1. The cost function used a hierarchical set of data and prior constraints to ensure that the inversion was both well-posed and produced reasonable profiles of all the relevant variables. The cost function and its components are,

$$M_{total} = \beta M_{data} + (1-\beta) M_{prior}, \tag{13}$$

$$M_{data} = \frac{1}{2}(M_u + M_{\dot{\epsilon}}), \tag{14}$$

$$M_{prior} = \frac{1}{3}(M_\tau + M_C + M_A), \tag{15}$$

$$M_u = RMS\left(\frac{u_{model} - u_{obs}}{u_{obs}}\right), \tag{16}$$

$$M_{\dot{\epsilon}} = RMS\left(\frac{\frac{du}{dx}_{model} - \frac{du}{dx}_{obs}}{\frac{du}{dx}_{obs}}\right), \tag{17}$$

$$M_\tau = n_\tau RMS\left(\frac{d^2\tau_b}{dx^2}\right), \tag{18}$$

$$M_C = n_C RMS\left(\frac{d^2 C}{dx^2}\right), \text{and} \tag{19}$$

$$M_A = \left(\frac{log(A_{long}) - log(A_0)}{\Delta A}\right)^2 + \left(\frac{max(0, log(A_{side}) - log(A_0))}{\Delta A}\right)^2 \tag{20}$$

where M_{total}, M_{data}, and M_{prior} are the total cost, data cost, and prior cost, respectively, M_u is the velocity data cost, $M_{\dot{\epsilon}}$ is the velocity gradient data cost, M_τ is the basal drag prior cost, M_C is the drag coefficient prior cost, M_A is the rate factor prior cost, $RMS()$ is the root-mean-square operator, n_τ and n_C are normalization parameters chosen to ensure that those prior costs have magnitudes of order 1, C is the drag coefficient, $A_0 = 5 \times 10^{-25}$ $\mathrm{Pa}^{-3}\mathrm{s}^{-1}$ is the default value of the rate factor, ΔA is an assumed range of uncertainty in the rate factor, and β is a tunable weighting parameter between 0 and 1. Note that for A_{long} we penalized both positive and negative deviations from the experimental value, but for A_{side} we wanted to allow weak shear margins so we only penalized the model if it was too strong. We use both velocity and strain rate in the data constraint to ensure that the model captures local structure in the width-averaged velocity field; however, these are not truly independent constraints and the choice to include both was arbitrary. We tested the sensitivity of the inversion to our choice of weighting parameter, β, and found that the results were relatively insensitive between values of approximately 0.3–0.7. We ran the inversion with β set at 0.5.

Once the inversion was performed, we used smoothed model drag and velocity to represent τ_0 and u_0, and then extrapolated those values beyond the present-day grounding line. An example of the inversion results is shown in the main text in Figure 3.

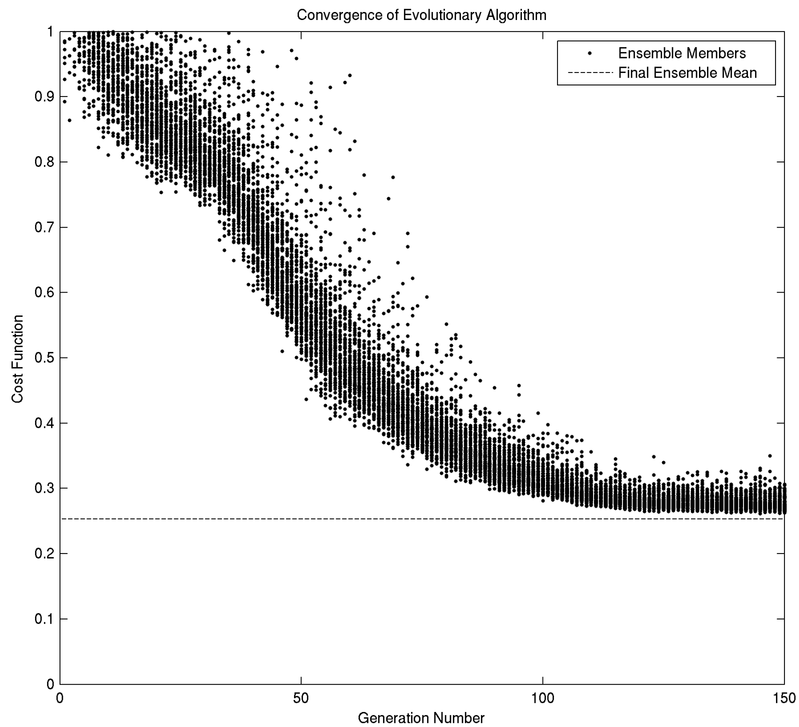

Figure 1: An example of the convergence of the evolutionary algorithm. Plot shows the cost function for every individual population member as a function of generation number. Note that the cost function for the final ensemble mean is lower than the cost function for any individual ensemble member.

2 Resolution Tests

The ability of ice models to simulate grounding line evolution is known to be dependent on grid resolution (Gladstone et al., 2017), so we ran resolution tests of our model against the analytical results of Schoof (Schoof, 2007). We used the polynomial overdeepened bed profile from that paper– which later became MISMIP experiment 3 (Pattyn et al., 2012)– in order to test whether our model could accurately capture the hysteresis loop associated with overdeepened bed geometries. The hysteresis associated with an overdeepened bed is a fundamental part of the Marine Ice Sheet Instability: in this hysteresis loop, stable steady states do not exist for a grounding line on a retrograde slope, only on the prograde slopes landward and seaward of it. As forcings are changed, the grounding line will resist crossing the overdeepening for as long as it can. The level of forcing required to make the grounding line retreat across the overdeepening is different than the level of forcing required to make it advance across the overdeepening, with a large swath of parameter space in the middle in which stable steady states are possible on either side of the overdeepening. The notion of societally–relevant "tipping points" for marine ice sheets in a warming climate is essentially an application of this mathematical concept to the real world: if the climate warms enough to force an ice sheet grounding line across the threshold into an overdeepening, then the grounding line will retreat rapidly, with a rapid simultaneous reduction in ice volume, and the climate would have to be cooled far below its present level to cause the ice sheet to advance again. Our results in this paper depend on the ability of our model to capture this dynamic behavior, so we explicitly used the hysteresis loop produced by an overdeepened bed geometry as the test case for the resolution tests.

For the test, we set flowband width to a uniform 1 m and we disabled side-drag. We varied grid resolution between 250 m and 32 km and we varied timesteps between 0.0625 yr and 8 yr. We changed both grid size and timestep by factors of 2 in between those extremes, for a total of 8 runs. The calving front was held at the end of the model domain throughout the experiment. We generated a full hysteresis loop by cycling accumulation from 20 cm/yr to 1 m/yr and back down again in steps of 10 ka. We lengthened the steps associated with jumps across the overdeepening to 20 ka to enable more sluggish low-resolution runs to cross the overdeepening as well (Fig S2). For each value of accumulation, we computed the true steady-state grounding line position by equating grounding line flux from (Schoof, 2007, eq.16) with integrated accumulation.

We found that the agreement between the model grounding line position and the analytical grounding line position improved as grid resolution improved (Figs S2, S3). The results showed a systematic increase in model sensitivity as resolution improved, such that low-resolution grounding lines migrated less in response to a change in forcing than high-resolution grounding lines (Figs S2, S3). Grid resolutions coarser than 4 km were not sensitive enough to make the jump across the overdeepening that is critical to defining the hysteresis loop, effectively producing a step change in model performance at this resolution. When resolution is better than this threshold (and when resolution is worse and the bifurcation point has not yet been reached) the error in grounding line position scales with the 0.6 power of grid resolution, while the error in ice volume scales roughly linearly with resolution (Fig S3). The model results presented in the rest of this paper were run with a nominal resolution of 500 m and a timestep of 0.02 yr. The timestep we used in the actual experiments was smaller than the one we used for the resolution tests because high sub–shelf melt rates produced steep slopes near the grounding line, which necessitated smaller timesteps to preserve numerical stability.

In addition to steady state grounding line position, we were also interested in testing the transient response of the model, since the results discussed in this paper depend strongly on transient grounding–line dynamics. To test the transient response, we used the highest resolution run to represent "truth", since an analytic solution for transient grounding line position does not exist. We used the rate of change during the bifurcation when the grounding line crosses the overdeepening to test the transient response, since the rate of migration across an overdeepened bed is the most important to the marine ice sheet instability. Both the error in grounding line migration rate and the error in sea level change rate scale roughly linearly with grid resolution (Fig S4).

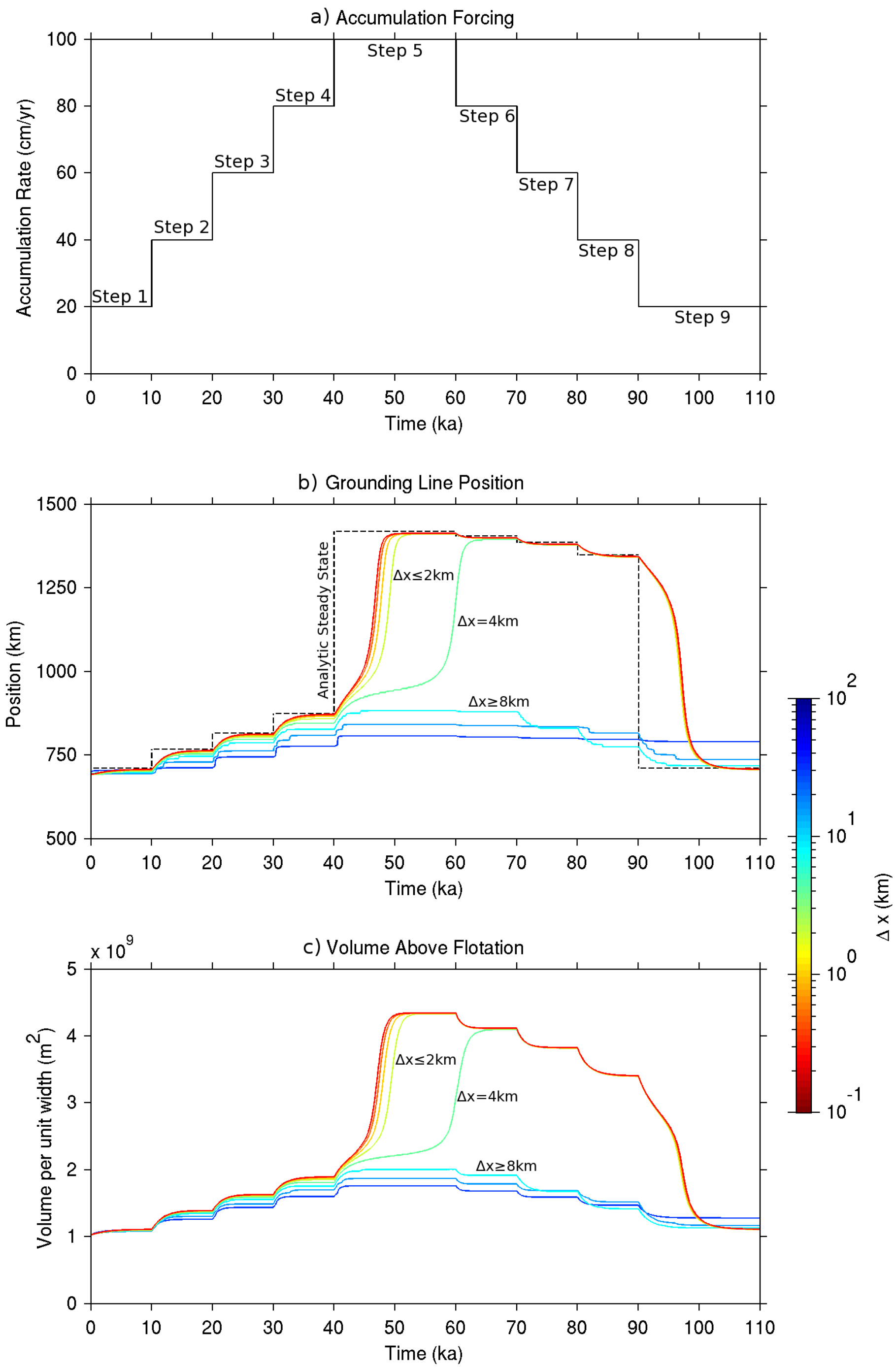

Figure 2: Resolution Tests Time Series: (a) accumulation rate forcing, (b) grounding line position, and (c) volume above flotation. Lines in (b) and (c) are colored by grid resolution. Dashed lines in (b) indicate analytic solution for grounding line position. Note that only runs with a resolution of 4 km or better are sensitive enough to cross the overdeepening, and even the 4 km run does only does so after a delay. The low sensitivity of the coarse runs can also be seen in their weaker response to small changes from 0-40 ka.

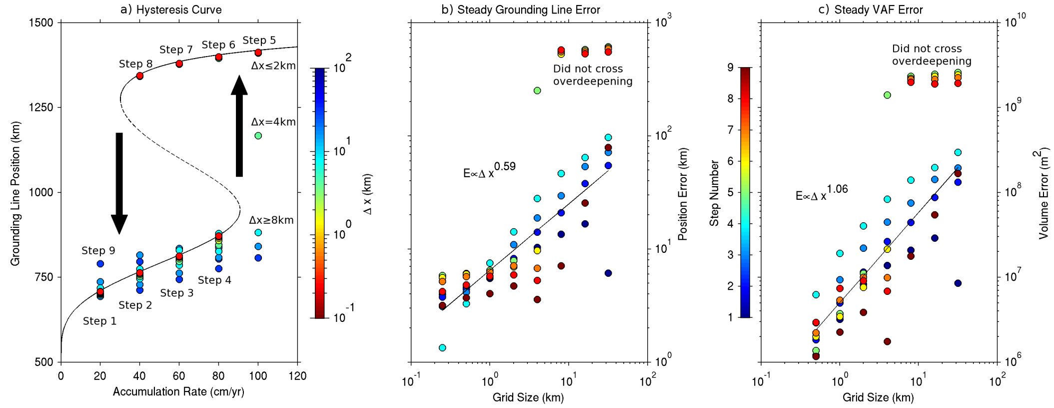

Figure 3: Resolution Tests Steady-State Error Analysis: (a) hysteresis loop, (b) grounding line errors, and (c) volume above flotation errors. Marker color in (a) represents grid resolution while marker color in (b) and (c) represent step number (Fig S2a). Black line in (a) indicates the analytic steady state solution, with solid lines representing stable solutions and dashed line representing unstable solutions. Arrows in (a) indicate the direction of the hysteresis loop in the experiment. Note that only runs with a resolution better than 4 km were sensitive enough to make the jump across the overdeepening in step 5 (and only runs with a resolution better than 2 km were done making the jump when the step completed). Runs that did not cross the overdeepening were excluded from the fit in panels (b) and (c).

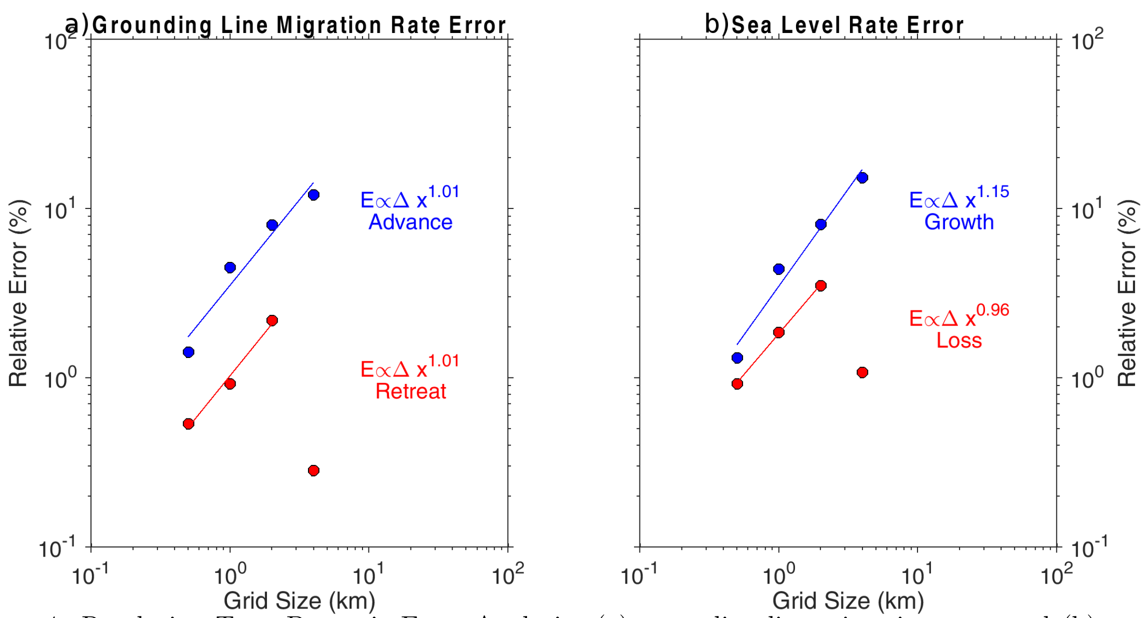

Figure 4: Resolution Tests Dynamic Error Analysis: (a) grounding line migration rate, and (b) sea level change rate. The highest resolution runs were taken to represent “truth” and separate fits were performed for the advance phase and for the retreat phase. In both cases, the rate being measured is the mean migration rate across the steepest part of the overdeepening, defined as those locations where the bed gradient is within a factor of 2 of the maximum overdeepened bed gradient.

3 Movies

We made animations showing model evolution for selected model runs. In each animation, light blue represents grounded ice, purple represents floating ice shelf, brown represents bedrock, gray represents the artificial sill (if present), and the ocean has been color–coded by temperature between -1.25°C and 1°C. Vertical lines within the ice are passive flow markers that advect with the ice velocity. Dashed lines represent the initial configuration of the glacier. We show five animations depicting various forcing scenarios associated with the experiment shown in Figure 5 of the main text: Animation 1 shows the warming scenario with no sill, Animation 2 shows the small sill with 0% water blockage, Animation 3 shows 50% water blockage (the same scenario shown in Figure 5 of the main text), Animation 4 shows 100% water blockage, and Animation 5 shows the large sill with 100% water blockage. The animations can be accessed at [URL].

References

Gladstone, R. M., Warner, R. C., Galton-Fenzi, B. K., Gagliardini, O., Zwinger, T., and Greve, R.: Marine ice sheet model performance depends on basal sliding physics and sub-shelf melting, The Cryosphere, 11, 319–329, https://doi.org/10.5194/tc-11-319-2017, 2017.

Jenkins, A.: A one-dimensional model of ice shelf-ocean interaction, Journal of Geophysical Research, 96, 20 671–20 677, 1991.

Jenkins, A.: Convection-driven melting near the grounding lines of ice shelves and tidewater glaciers, Journal of Physical Oceanography, 41, 2279–2294, https://doi.org/10.1175/JPO-D-11-03.1, 2011.

Joughin, I., Tulaczyk, S., Bamber, J. L., Blankenship, D., Holt, J. W., Scambos, T., and Vaughan, D. G.: Basal conditions for Pine Island and Thwaites Glaciers, West Antarctica, determined using satellite and airborne data, Journal of Glaciology, 55, 245–257, https://doi.org/10.3189/002214309788608705, 2009.

Pattyn, F., Schoof, C., Perichon, L., Hindmarsh, R. C. A., Bueler, E., de Fleurian, B., Durand, G., Gagliardini, O., Gladstone, R., Goldberg, D., Gudmundsson, G. H., Huybrechts, P., Lee, V., Nick, F. M., Payne, A. J., Pollard, D., Rybak, O., Saito, F., and Vieli, A.: Results of the Marine Ice Sheet Model Intercomparison Project, MISMIP, The Cryosphere, 6, 573–588, https://doi.org/10.5194/tc-6-573-2012, 2012.

Rignot, E., Mouginot, J., and Scheuchl, B.: Ice flow of the Antarctic Ice Sheet, Science, 333, 1427–1430, https://doi.org/10.1126/science.1208336, 2011.

Schoof, C.: Ice sheet grounding line dynamics: Steady states, stability, and hysteresis, Journal of Geophysical Research- Earth Surface, 112, https://doi.org/10.1029/2006JF000664, 2007.

Sergienko, O. V.: The effects of transverse bed topography variations in ice-flow models, Journal of Geophysical Research: Earth Surface, 117, n/a–n/a, https://doi.org/10.1029/2011JF002203, 2012.

Weertman, J.: On the sliding of glaciers, Journal of Glaciology, 3, 33–38, 1957.